Global TEC maps based on GNSS data: 1. Empirical background TEC model

P. Mukhtarov,[1] D. Pancheva,[1] B. Andonov,[1] and L. Pashova[1]

Received 17 January 2013; revised 18 April 2013; accepted 19 June 2013.

[1] A global background total electron content (TEC) model is built by using the Center for Orbit Determination of Europe (CODE) TEC data for full 13 years, 1999–2011. It describes the climatological behavior of the ionosphere under both its primary external driver, i.e., the direct photo-ionization by incident solar radiation, and regular wave particularly tidal forcing from the lower atmosphere. The model construction is based on the very different time scales of the solar cycle, seasonal, and diurnal TEC variabilities (at least an order of magnitude); this leads to modulations of shorter-period variabilities with periods of the longer ones. Then the TEC spatial-temporal variability is presented as a multiplication of three separable functions. The solar activity is described by both parameters: F10.7 and its linear rate of change K_F while the seasonal variability is presented by sine functions including four subharmonics of the year. The diurnal variability of the TEC model is described by 2D (longitude-time) sine functions with zonal wave numbers up to 4 and 4 subharmonics of the solar day. The model offers TEC maps which depend on geographic coordinates (5°×5° in latitude and longitude) and UT at given solar activity and day of the year. The presented background model fits to the CODE TEC input data with a zero systematic error and an *RMS* error of 3.387 TECU. It is able to reproduce the well-known ionospheric structures as Weddell Sea Anomaly and some longitudinal wave-like structures.

Citation: Mukhtarov, P., D. Pancheva, B. Andonov, and L. Pashova (2013), Global TEC maps based on GNSS data: 1. Empirical background TEC model, *J. Geophys. Res. Space Physics*, *118*, doi:10.1002/jgra.50413.

1. Introduction

[2] The conventional sources of ionospheric structure and variability are related to changes in solar extreme ultraviolet (EUV) and ultraviolet (UV) radiation and geomagnetic activity, together with the subsequent response of the thermosphere-ionosphere system and interaction between the components [*Roble*, 1995]. The ionosphere also varies in response to neutral winds that move ions and electrons along inclined magnetic field lines [*Schunk and Nagy*, 2009], electrodynamical coupling with the overlying plasmasphere and magnetosphere [*Huba et al*., 2005], and dynamical coupling with the underlying atmosphere particularly effective during low solar activity conditions [*Mendillo et al*., 2002; *Rishbeth*, 2006]. The high sensitivity of the ionosphere to the external forcing and the continuous action of the lower atmospheric forcing causes significant ionospheric variability on different time and spatial scales. To understand and forecast such variability is one of the main tasks of space weather research.

[3] Ionospheric models have been playing an important role for many years in specifying the ionospheric environment through which the radio waves propagate as realistically as possible. These ionospheric models can be classified into three main categories [*Feltens et al*., 2011]: (i) first principles models (physical models) based on ionospheric physics and chemistry [*Schunk et al*., 1986; *Fuller-Rowell et al*., 1987]; (ii) parametric models which simplify the physical models reducing the number of parameters [*Anderson et al*., 1989; *Daniell et al*., 1993a, 1993b], and (iii) empirical models based on observations [*Hedin et al*., 1996; *Drob et al*., 2008]. The present two companion papers are devoted to empirical modeling and that is why this type of models is going to be discussed further. Ionospheric empirical models are established on statistical analysis of long-term data sets and utilize appropriate functions to describe the intrinsic variations of the ionospheric parameters. They usually represent the main features of the ionosphere quite well, but are limited to the way the model was constructed, the used data, and the conditions occurring while the data set was taken [*Ercha et al*., 2012]. These models are often formulated in terms of monthly median parameters and represent the state of the ionosphere for a particular epoch of solar activity. Hence, they can describe and predict the long-time average conditions of the ionosphere and are usually used for planning radio system operations. A typical example of a monthly median empirical model is the International Reference Ionosphere (IRI) [*Bilitza*, 2001; *Bilitza and Reinisch*, 2008].

This article is a companion *to Mukhtarov et al*. [2013], doi:10.1002/jgra.50412.

[1]National Institute of Geophysics, Geodesy and Geography, Bulgarian Academy of Sciences, Sofia, Bulgaria.

Corresponding author: P. Mukhtarov, National Institute of Geophysics, Geodesy and Geography, Bulgarian Academy of Sciences, Sofia, Bulgaria. (dpancheva@geophys.bas.bg)

2169-9380/13/10.1002/jgra.50413

[4] Among ionospheric parameters, the total electron content (TEC) is one of the particularly important physical quantities of the ionosphere. TEC has been extensively investigated and modeled for both scientific research of ionosphere and for applications. The main reason for the TEC importance is that the trans-ionospheric radio signals, used by the Global Navigation Satellite Systems (GNSS), may experience quiet large range errors, and these errors are proportional to the integral of the electron density along the ray path, i.e., proportional to slant TEC. In this way, the ionospheric effect has become the largest error source in GNSS positioning, timing, and navigation. Hence, the accuracy of the GNSS such as the Global Positioning System (GPS), the Russian GLONASS, the Chinese BeiDou, and the European Galileo is heavily affected by the ionosphere. Under normal solar activity conditions, the ionospheric influence on GPS signals is usually in the range from a few meters to tens of meters, but it could reach more than 100 m during severe ionosphere storms [*Gao and Liu*, 2002]. Using the dispersive properties of the ionosphere, it is possible to eliminate most of this error, or so called first-order range error, by differential measurements in dual-frequency systems like GPS, 1575.42 MHz at L1 and 1227.60 MHz at L2. However, ionosphere dual-frequency algorithms used for positioning applications remove only first-order range error [*Brunner and Gu*, 1991] but do not take into account its higher-order terms. Also, the ray paths and TEC are assumed to be the same for both frequencies which is away from the reality particularly considering the horizontal gradients of the ionosphere electron density [*Kashcheyev et al*., 2012]. Additionally, there are still numerous single-frequency applications which need additional information for mitigating the ionospheric propagation error. Such GNSS users can be provided by adequate ionospheric corrections obtained by an autonomous ionospheric TEC model (without any ionospheric measurements). Recently, for precise GNSS applications, higher-order ionospheric terms are considered and taken into account especially at higher solar activity [*Hoque and Jakowski*, 2007; *Elmas et al*., 2011].

[5] TEC empirical models can be constructed by the following two different ways: (i) from existing empirical models of the electron density distribution such as IRI [*Bilitza and Reinisch*, 2008] or NeQuick [*Hochegger et al*., 2000; *Radicella and Leitinger*, 2001; *Nava et al*., 2008], which describes the profile of electron density and is driven by geographic/geomagnetic location, F10.7, and geomagnetic activity level, and (ii) by using different TEC measurements at single, regionally and globally distributed sites. Most early empirical TEC models were constructed on the basis of three different techniques for measuring the ionospheric TEC: Faraday rotation, Differential Doppler, and Group Delay methods. Some details about the models built on the TEC data from the above mentioned techniques can be found in *Mao et al*. [2008] and *Ercha et al*. [2012] and the references therein.

[6] Recently, the GPS measurements obtained from the global and regional networks of International GNSS Service (IGS) ground receivers have become a major source of TEC data over large geographic areas [*Wilson et al*., 1995; *Komjathy*, 1997; *Mannucci et al*., 1998; *Hernández-Pajares et al*., 1999; *Orús et al*., 2005]. The GPS has become a powerful measurement tool to investigate the global and regional ionospheric structures owing to its continuous, easy operation, and worldwide distributed receivers. This system offers low-cost information characterized by its accuracy, high temporal and spatial resolution, and availability. The GPS technique has great advantage in producing real-time global ionosphere maps (GIMs) and regional ionosphere maps (RIMs) of TEC distribution by using different methods [*Iijima et al*., 1999; *Ping et al*., 2002; *Otsuka et al*., 2002; *Meggs et al*., 2004; *Orús et al*., 2005; *Stolle et al*., 2005; *Fuller-Rowell et al*., 2006; *Zapfe et al*., 2006; *Sayin et al*., 2008]. Therefore, many new TEC empirical models based on the instantaneous snapshots of the global/regional ionospheric TEC represented by GIMs/RIMs have been well developed. For example, *Mao et al*. [2008] built a climatological model of TEC over China using nine years (1996–2004) of GPS data and utilizing empirical orthogonal function (EOF) analyses. *Lean et al*. [2011a] reported a linear model that includes solar EUV irradiance variations (0–103 nm), four oscillations (at semiannual, annual, terannual, and biennial periods), geomagnetic activity, and a positive long-term trend [*Lean et al*., 2011b] which capture more than 98% of the variance in the GPS-derived daily averaged global TEC during the period from 1995 to 2010. Using historical estimates of solar EUV irradiance and geomagnetic activity, this model also facilitates the reconstruction of TEC climatology in the past, which has been illustrated since 1950. *Ercha et al*. [2012] constructed a global empirical TEC model based also on EOF analysis and by using the GIMs provided by Jet Propulsion Laboratory (JPL) during the years 1999–2009. *Bouya et al*. [2010] used Spherical Cap Harmonic Analysis to construct a regional ionospheric TEC model over Australia. *Habarulema et al*. [2010, 2011] built regional GPS-based TEC models over Southern Africa by using a neural network analysis method. *Wan et al*. [2012] developed a global ionospheric TEC model using a statistical Eigen mode analysis method. In this way, the GPS-based ionospheric TEC data have been extensively utilized recently in ionospheric studies to analyze and validate the ionospheric models and for space weather monitoring applications.

[7] The basic aim of the present paper (Part 1) is to present a global empirical background TEC model which is built by using long-term TEC data from the Center for Orbit Determination of Europe (CODE) [*Schaer*, 1999]. The main purpose is to describe the mean behavior of the ionosphere under both its primary external driver, i.e., the direct photo-ionization by incident solar radiation, and regular wave particularly tidal forcing from the lower atmosphere. Moreover, we aim to make this model applicable under quiet geomagnetic conditions for long-term prediction of the average TEC variability. Not only a detailed statistical evaluation of the global empirical background TEC model is accomplished in Part 2, but an error model is established as well; the latter differentiates the present empirical model from others.

2. TEC Data Set

[8] The ionospheric TEC is derived by mapping the slant path delay of the signal from dual-frequency L1 and L2 bands observed by the global networks of IGS ground receivers [*Ge et al*., 2004; *Dow et al*., 2009]. IGS provides the highest precision of GPS satellite orbits, and precise positions (5 mm) for 350 worldwide reference stations [*Ercha et al*., 2012]. Usually, the single ionospheric layer

assumption is considered to convert the slant path TEC to vertical TEC with a mapping function. Currently, five analysis centers routinely provide GIMs of vertical TEC using the growing global network of dual-frequency GNSS receivers [*Ercha et al*., 2012]. These are CODE [*Schaer*, 1999], JPL [*Ho et al*., 1996], European Space Agency [*Feltens and Schaer*, 1998; *Feltens*, 2007], Polytechnical University of Catalonia [*Hernández-Pajares et al*., 1997], and the Energy Mines and Resources Canada [*Gao et al*., 1994].

[9] It has been already mentioned that the present background TEC model is constructed on the base of TEC maps generated by the CODE at Astronomical and Physical Institutes of the University of Bern (http://cmslive3.unibe.ch/unibe/philnat/aiub/content/e15/e59/e126/e440/e447/index_eng.html). For the current study, we chose data for full 13 years, 1 January 1999 – 31 December 2011, provided from the CODE FTP directory: ftp://ftp.unibe.ch/aiub/CODE/. At CODE, the vertical TEC is modeled with a spherical harmonic expansion up to degree of order 15 referring to a solar-geomagnetic reference frame [*Schaer*, 1999]. The two-hourly sets are derived from GPS data of the global IGS network of about 200 stations. The GIM/CODE is regarded as one of the most precise TEC maps generated from GNSS observations. The used global IGS TEC data have a time resolution of 2 h and a grid spacing of 5° × 2.5° in longitude and latitude, respectively, with errors of several TEC Units (TECU, 1 TECU = 10^{16} el/m^2) [*Hernández-Pajares et al*., 2009]. The errors of the GIM/CODE are determined by comparing with an independent source of TEC. The reference TEC values are provided by dual-frequency altimeters on board of TOPEX, JASON, and ENVISAT satellites. Because the altimeters are working over oceans, this comparison is considered as a pessimistic determination of the global TEC map actual errors.

[10] The original global TEC data were arrayed in terms of the coordinate system of geographical latitude (from −87.5° to 87.5° at each 2.5°) and longitude (from −180° to 180° at each 5°). It is known, however, that the neutral wind and electric field effects on the ionosphere are dependent on the geomagnetic field configuration as the electrons are constrained to the magnetic field lines. That is why the distribution of the ionospheric parameters, including TEC as well, is usually presented in geomagnetic latitude instead of geographic one. Early investigations [reported, e.g., in *Rawer*, 1984] demonstrated the benefit of using the modified dip (modip) latitude, introduced by *Rawer* [1963], to describe the variability of the densest part of the ionosphere, particularly at mid and low latitudes. The modip latitude which is adapted to the real magnetic field, e.g., to the magnetic inclination (dip), is defined by: $\tan\mu = I \Big/ \sqrt{\cos\Phi}$, where μ is the modip latitude, I is the true magnetic dip (usually at a height of 350 km), and Φ is the geographic latitude. Modip equator is the locus of points where the magnetic dip (or inclination) is 0. In the equatorial zone, the lines of constant modip are practically identical to those of the magnetic inclination, but as latitude increases, they deviate and come nearer to those of constant geographical latitude. The poles are identical to the geographic ones [*Azpilicueta et al*., 2006]. Then for the purpose of this study, the global TEC data were rearrayed in terms of the coordinate system of modip latitude, from −80° to 80° at each 5°, and geographic longitude, from −180° to 180° at each 15°. The TEC data falling into the area 5° (modip latitude) × 15° (longitude) were averaged.

[11] Usually the background ionospheric models are formulated in terms of monthly median parameters because such parameters are not affected by large but short-time lasting disturbances generated by strong geomagnetic storms. In the present study, we use sliding medians defined by a 31 day moving window, and the median value is assigned to the central day of the window, i.e., to the 16th day of the window. The sliding medians are calculated independently for each point of the grid (as it is done with single station data). In this way, the daily TEC time series are obtained at each modip latitude, longitude, and UT. It is worth noting that the perturbations from geomagnetic origin or related to solar rotation period are filtered from these time series.

3. Basic Approach of the Model Construction

[12] The basic idea of each global empirical background TEC model, used for long-term prediction, is to define a set of empirical functions which describes the most probable TEC values at given solar activity, day of the year (DOY), geographic location, and UT. In the present study, we accepted: (i) longitude and UT as independent variable quantities; the conversion into local time (LT) is a simple procedure, and (ii) at each modip latitude, a separate model is constructed; the values of the model TEC which do not belong to the 5° modip grid are obtained by an interpolation procedure that will be described later. The latter is done because if a latitudinal approximation is used, first the number of model constants will increase, and second an additional error will be introduced in the model.

[13] According to the above mentioned approach, the TEC values at each modip latitude circle can be presented as a function of:

$$TEC(solar\ activity, DOY, longitude, UT) \tag{1}$$

[14] Ideally, the solar activity should be described by an index that tracks the solar cycle changes in the EUV wavelength range, since this part of the solar spectrum affects the ionosphere (Bilitza, 2001). However, such indices cannot be observed at the ground and are only available for relatively short time periods covered by satellite UV instruments. Actually recently *Lean et al*. [2011c] have reported new models (two and three components) of solar EUV irradiance variability (from 0 to 120 nm), by using multiple regression of the Mg II and F10.7 solar activity indices with irradiance observations made during the descending phase of solar cycle 23. The authors used the Solar EUV Experiment on the Thermospheric Ionospheric Mesospheric Energy and Dynamics (TIMED) spacecraft observations of solar EUV irradiance. The models have been used to reconstruct EUV spectra daily since 1950, annually since 1610, to forecast daily EUV irradiance, and to estimate future levels in cycle 24. These models, however, have not yet been openly accessible for the scientific community. Thus, most ionospheric modelers use the sunspot number (number of dark spots on the solar disc) and the solar radio flux at 10.7 cm wavelength (F10.7) as solar indices, since both can be observed from the ground, long data records exist, and they can be predicted. These indices together with their 6 month predictions are

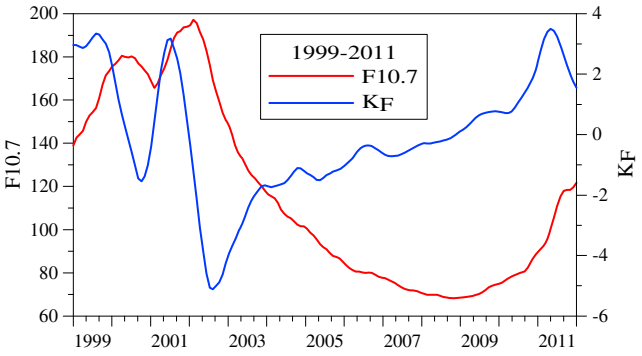

Figure 1. Monthly mean solar radio flux *F10.7* (red line) and its linear rate of change K_F (blue line) obtained by a sliding 11 month time derivatives of *F10.7*.

regularly published by NOAA Space Weather Prediction Center (http://www.swpc.noaa.gov/index.html). Some preliminary experiments were preformed with both indices, and the results revealed that particularly for the considered last solar cycle F10.7 describes better the TEC variability. Thus, in the present study, F10.7 is used as a proxy for the solar activity. It is known, however, that the ionosphere behaves differently at the rising and declining phases of the solar cycle at one and the same F10.7, i.e., at one and the same F10.7, the TEC values in the rising and in the falling part of the solar cycle are different [*Huang*, 1963; *Gopal Rao and Sambasiva Rao*, 1969; *Apostolov et al*., 1994]. To include this ionospheric feature in the model, an additional parameter K_F is used which describes the linear rate of change of F10.7. The idea for describing the solar activity by such two parameters, i.e., by the level of solar activity and its tendency, was introduced for the first time by *Pancheva and Mukhtarov* [1996] in modeling the monthly median critical frequency of the ionospheric *F* region, f_oF2, above Sofia. Later, this idea was used for long-term prediction of other ionospheric parameters, and the model approach was successfully applied to other European ionosonde stations [*Pancheva and Mukhtarov*, 1998]. It was found that the inclusion of the K_F in the monthly median f_oF2 model decreased its mean standard deviation by ~0.5 MHz. Figure 1 shows the temporal variability of the used two solar parameters *F10.7* in solar flux units (10^{-22} W m^{-2} Hz^{-1}) and K_F for the considered 13 years (1999–2011). It can be distinguished that this solar cycle is characterized by double-peak solar maximum; while the first peak occurs in 2000, the second one is seen in 2002.

[15] The seasonal variability of the vertical TEC is characterized mainly by annual and semiannual components [*Natali and Meza*, 2011] whose amplitudes and phases depend on solar activity, geographic/geomagnetic location and UT. The seasonal components with periods shorter than 6 months have also some contribution, but they are weaker than annual and semiannual components. In general, the semiannual behavior is characterized by a larger peak in March–April than that in September–October; the difference is particularly strong (up to 40%) during high solar activity [*Natali and Meza*, 2011].

[16] In all existing so far empirical models, the diurnal TEC variability is described only by the migrating "tidal" components, i.e., components with periods 24, 12, 8 h, etc., which propagate with the apparent motion of the Sun to a ground-based observer. In this way, it is assumed that the diurnal variability of the ionosphere is forced mainly by the diurnal cycle of the photo-ionization. However, only within the past 5–6 years has the realization emerged that "troposphere weather" contributes significantly to the "space weather" of the thermosphere, especially during solar minimum conditions. Much of the attendant variability is attributable to upward-propagating solar tides excited by latent heating due to deep tropical convection, and solar radiation absorption primarily by water vapor and ozone in the troposphere and stratosphere, respectively. Recent studies based on the modern satellite-board data (electron densities from COSMIC and temperatures from TIMED) revealed that while the ionospheric migrating semidiurnal tidal (SW2, S for semidiurnal, W means westward, and 2 clarifies the wave number) response is predominantly shaped by the migrating SW2 tide forced from below, the migrating diurnal tidal (DW1, D for diurnal) response is mainly due to daily variability of the photo-ionization [*Pancheva and Mukhtarov*, 2012]. The nonmigrating tides which amplify in the lower thermosphere are particularly important for the ionosphere. Through coupling mechanisms (such as the wind dynamo), they can play an important role in generating the longitudinal variability in the ionosphere. A special attention has been paid recently on the nonmigrating tides DE3 and DE2 (diurnal eastward propagating tides with zonal wave numbers, respectively, 3 and 2) as a link between the troposphere and ionosphere [*Immel et al*., 2006; *Kil et al*., 2008; *Hartman and Heelis*, 2007; *Ren et al*., 2008; *Wan et al*., 2008; *Pancheva and Mukhtarov*, 2010]. *Mukhtarov and Pancheva* [2011] investigated in detail the ionospheric response to the above mentioned nonmigrating tides by using COSMIC global electron density data. Later, their experimental results have been supported by the numerical simulations done with the recently developed Earth's whole atmospheric model from the troposphere to the ionosphere, called GAIA [*Pancheva et al*., 2012]. The above mentioned effects of the tidal forcing which induce longitude variability are not yet emulated in empirical ionospheric models. In the present study, we include these influences.

[17] There is another reason also for including the nonmigrating tidal variability in the TEC model. It is related to the offset between the geographic and modip latitudes. The dynamics of the thermosphere (defined mainly by prevailing winds and atmospheric tides) is defined in a geographic frame, but its effect on the ionosphere depends on the geomagnetic field configuration. The photo-ionization depends also on geographic frame (solar zenith angle); however, as the electrons are constrained to the magnetic field lines, its effect is geomagnetic field dependent. The offset between geographic and geomagnetic frames generates additional tidal ionospheric responses which can originally not be present in the forcing from below. These additional ionospheric tides are much weaker than the real ones (on the average ~3–10%), but they have some contribution to the diurnal variability of the ionosphere particularly in shaping some quasi-stationary structures.

[18] As the time scales of the solar cycle, seasonal, and diurnal influences on the TEC variability are very different (they differ at least an order of magnitude), then the shorter-period TEC variabilities are usually modulated by the longer ones. In this case, the TEC spatial-temporal variability can be represented as a multiplication of three

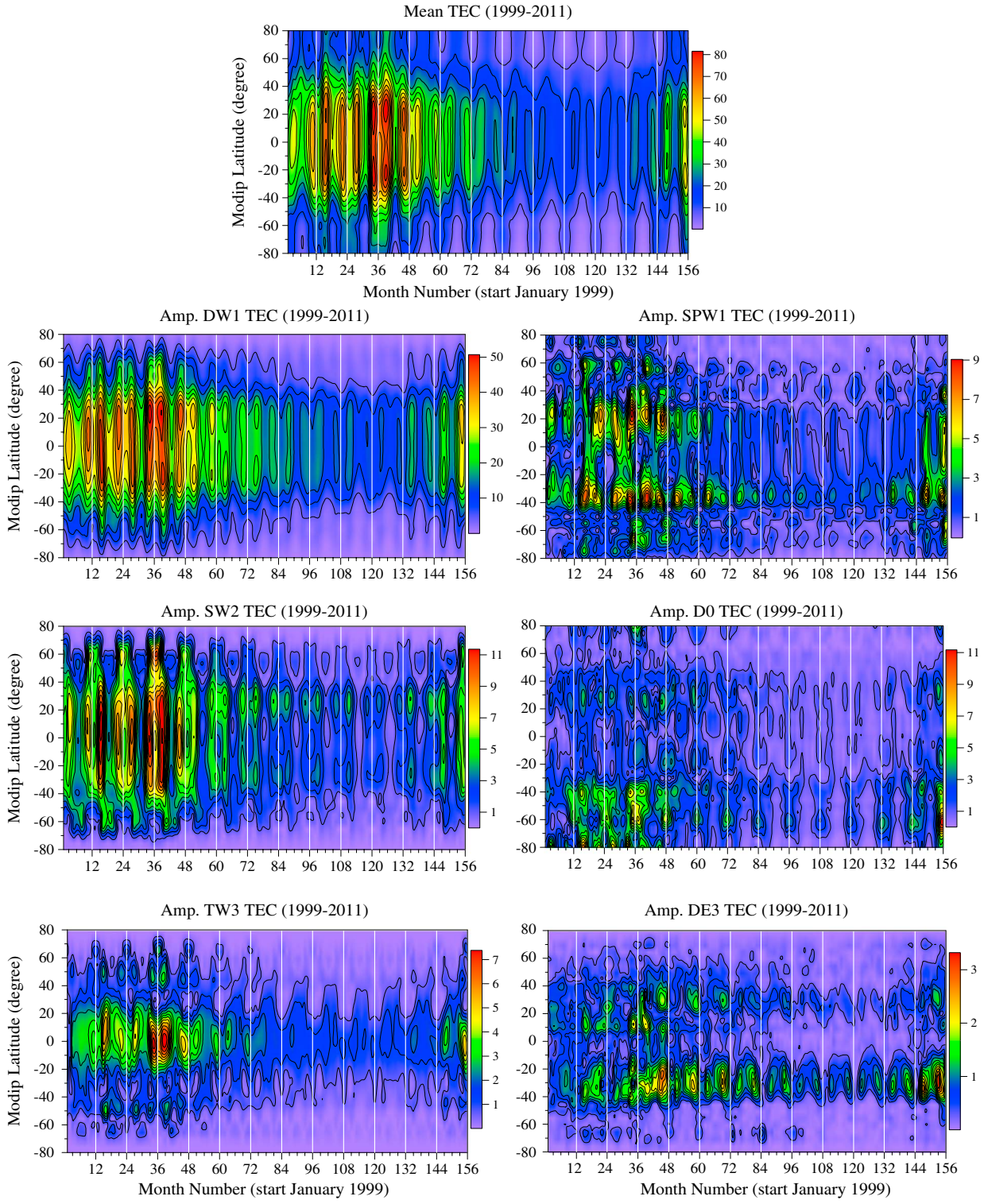

Figure 2. Latitude-time cross sections of the following TEC components: (i) zonal and time mean TEC (upper most plot); (ii) left column of plots shows the amplitudes of migrating diurnal (DW1, upper plot), semidiurnal (SW2, middle plot), and terdiurnal (TW3, bottom plot) tides, and (iii) right column of plots shows the amplitudes of SPW1 (upper plot), nonmigrating zonally symmetric diurnal tide (D0, middle plot) and nonmigrating eastward propagating tide with zonal wave number 3 (DE3, bottom plot). The considered years from 1999 to 2011 are separated by thin white lines; the TEC components are measured in TECU.

separable functions, i.e., (1) can be expressed in the following way [*Pancheva et al*., 2005]:

$$TEC(F, K_F, DOY, lon, UT) = \Phi_1(F, K_F)\,\Phi_2(DOY)\,\Phi_3(lon, UT) \quad (2)$$

[19] The above right-hand side unknown functions Φ_k $(k = 1,2,3)$ can be represented by their series expansions; Φ_1 can be expanded in Taylor series, while Φ_2 and Φ_3, which are periodic functions with periods, respectively, a year and a solar day, can be expanded in Fourier series. Therefore, the background TEC model can be described by the following functions:

$$\begin{aligned} TEC(F, K_F, DOY, lon, UT) &= \left(\alpha_0 + \alpha_1 F + \alpha_2 K_F + \alpha_3 F K_F + \alpha_4 F^2 + \alpha_5 {K_F}^2\right) \\ &\times \left(\beta_0 + \sum_{i=1}^{4} \beta_i \cos\left(i\frac{2\pi}{365} day - \varphi_i\right)\right) \\ &\times \left(\gamma_0 + \sum_{i=1}^{4}\sum_{s=-4}^{4} \gamma_{is} \cos\left(i\frac{2\pi}{24} UT - s\frac{2\pi}{360} lon - \psi_{is}\right)\right. \\ &\left. + \sum_{s=1}^{4} \delta_s \cos\left(s\frac{2\pi}{360} lon - \zeta_{is}\right)\right) \end{aligned} \quad (3)$$

[20] The expression in the first right-hand bracket, i.e., the Taylor series expansion up to degree of 2, represents the solar activity term which modulates the seasonal and diurnal behavior of the ionosphere. The seasonal term (expression in the second right-hand bracket) includes four subharmonics of the year, i.e., annual, semiannual, 4, and 3 month components; it modulates the diurnal behavior of the ionosphere. The diurnal variability of the TEC model (expression in the third right-hand bracket) is composed by three parts: mean TEC (γ_0), a part describing migrating and nonmigrating tides, and a part representing the effect of the stationary planetary waves (SPWs). The contribution of the migrating and nonmigrating tides is presented by 2D (longitude-time) sine functions with zonal wave numbers up to 4 and subharmonics of the solar day with periods 24, 12, 8, and 6 h. The last part, describing the contribution of the SPWs, includes waves with zonal wave numbers up to 4. The presence of these wave structures in the ionosphere can be related to a few reasons: (i) offset between geographic and modip frames; (ii) can be generated by coupling processes between migrating and nonmigrating tides with one and the same periods [*Oberheide et al*., 2011], and (iii) some effect of the SPW1 temperature field in the lower thermosphere on the ionosphere, particularly at middle-high and high-latitude ionosphere; *Mukhtarov et al*. [2010] found strong evidence indicating that the auroral heating is a main origin of the lower thermospheric SPW1 structure.

[21] The background TEC model described by (3) contains 4374 constants, and they are determined by least squares fitting techniques. The numbers of the included components in the above described Taylor and Fourier expansion series are defined experimentally. The above mentioned solar, seasonal, and diurnal components have been determined on the basis of trial and error method by using the following criterion: the addition of more components has been discarded when their inclusion leads to an error improvement only after the third decimal point.

[22] Figure 2 presents examples of solar cycle and seasonal modulations of some diurnal components included in the TEC model. For this purpose, the TEC data are decomposed to mean TEC, migrating and nonmigrating tides, and SPWs (i.e., expressions in the third right-hand bracket of (3)) by using a 31 day window. Then the 31 day window is moved forward through the time series with steps of 1 day in order to obtain the daily values of the wave characteristics for period of time 1 January 1999–31 December 2011. The monthly mean wave characteristics, shown in Figure 2, are obtained by vector averaging for each calendar month [*Pancheva and Mukhtarov*, 2012]. We note that the color scale of Figure 2 and all other figures is in TECU. The uppermost plot shows the latitude-time cross section of the zonal and time mean of the TEC (first term, γ_0, in the third bracket); the considered years from 1999 to 2011 are separated by thin white lines. This diurnal TEC component follows strictly the solar activity, even the two maxima, a main maximum in 2002 (~80 TECU) and a secondary one in 2000 (~75 TECU), can be clearly distinguished. The semiannual variability is a dominant component of the seasonal behavior; on the average, the vernal equinox maxima are stronger than the autumnal ones. The left column of plots present the latitude-time cross sections of the first three migrating tides, 24 h (DW1, upper plot), 12 h (SW2, middle plot), and 8 h (TW3, bottom plot). The DW1 component is the strongest tidal component (maximum amplitude reaches ~50 TECU) and is shaped mainly by the diurnal variability of the photo-ionization. The SW2 component is significantly weaker than the DW1 one (maximum amplitude reaches ~11 TECU) and as it has been already mentioned is formed mainly by the SW2 tide forced from the lower atmosphere [*Pancheva and Mukhtarov*, 2012]. A clear evidence for the dominant role of the lower atmospheric SW2 tide on the TEC SW2 variability is the existence of the local winter maxima at modip latitude around ±60°. *Wu et al*. [2011] investigated the mesosphere-lower thermosphere SW2 tide in the neutral winds measured by the instrument TIDI on board of the TIMED satellite and found that at high latitudes the SW2 amplifies in winter solstice. The solar cycle and seasonal (mainly semiannual) modulations can be seen well for these diurnal components as well. While at high solar activity, the separation at both sides of the equator can be well seen for the mean (γ_0) and DW1 components, for the SW2 component, such separation is evident better at low solar activity; at high solar activity, the SW2 amplifies predominantly over the equator. The amplifications of the mean TEC, tidal DW1, and SW2 amplitudes around ± (20–30°) modip are related to the equatorial ionization anomaly (EIA) observed mainly during the daytime. Figure 2 shows that the solar activity affects not only the amplitude of the TEC EIA but also the location of the crests; at high solar activity, they are located close to ±30°, while at low solar activity, the crests move close to the equator, around ±20°. The solar cycle and seasonal modulations are seen also on the third migrating component, TW3. The latitude structure of this diurnal component shows a main amplification over the equator and secondary ones around ±50° and ±65°; the latter are particularly well seen during high solar activity.

[23] The right column of plots present the latitude-time cross sections of the amplitudes of the SPW1 (upper plot), nonmigrating zonally symmetric diurnal (D0, middle plot)

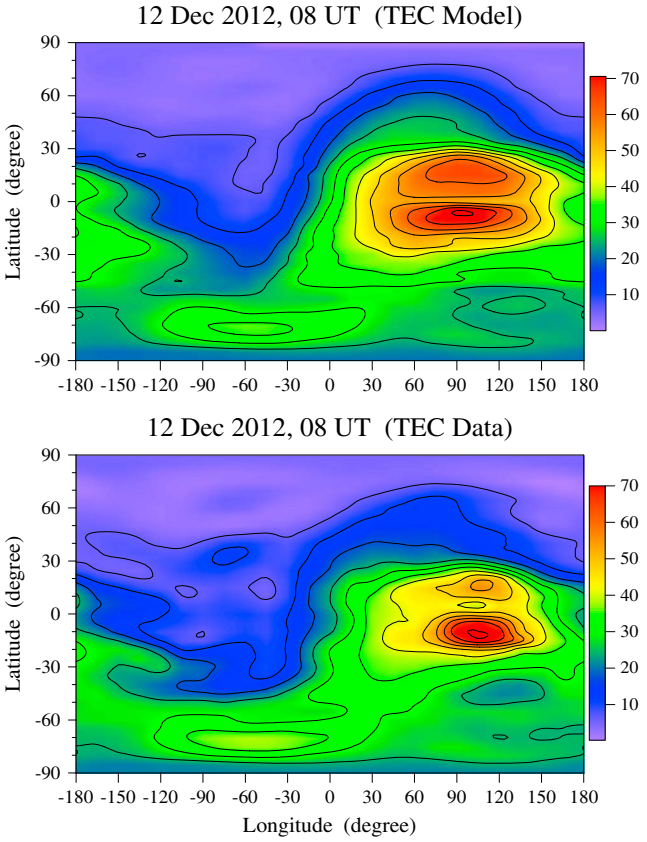

Figure 3. Global map in geographical frame calculated from the empirical background TEC model (upper plot) compared with the CODE TEC map (bottom plot) at 08 UT for 12 December 2012; the Weddell Sea Anomaly is apparent between −80° to −50° S and −120° to 0° E.

and nonmigrating eastward propagating diurnal tide with zonal wave number 3 (DE3, bottom plot). All these diurnal components demonstrate regular solar cycle and seasonal variability. Their amplitudes are weaker than the DW1 tide but are comparable with those of the SW2 and TW3 tides. The D0 is the strongest nonmigrating component with maximum amplitude of ~11 TECU (the same as that of SW2). It amplifies mainly in the Southern Hemisphere (SH) at high latitudes; similar distributions have also the other zonally symmetric tidal components, but their amplitudes are weaker than that of D0 (not shown here). All zonally symmetric tidal components show amplifications like stripes between −40° and −70° modip latitude that can be distinguished even at low solar activity. Similar amplifications are evident for SPW components, but they are present at both hemispheres. Later, it will be shown that just these zonally symmetric nonmigrating and SPW components have predominant contribution to the so called Weddell Sea Anomaly (WSA) [*He et al*., 2009; *Chen et al*., 2011]. This anomaly appears as an evening enhancement in electron density, i.e., larger nighttime electron density than during the day, in the region near the Weddell Sea, Antarctica peninsula. The WSA occurs mostly in southern summer and can extend from South America and Antarctica to the central Pacific.

[24] The TEC DE3 component (bottom plot), similarly to the other diurnal components, is strongly modulated by the solar cycle and shows clear semiannual variability. In this case, however, the autumnal maxima are stronger than the vernal ones. This is due to fact that the neutral DE3 tide forced from below is the main driver of the ionospheric DE3 variability. Recent studies on the temperature and neutral wind DE3 tide based on the satellite measurements revealed that this tide amplifies at lower thermosphere (~105–110 km) during August–October [*Oberheide and Forbes*, 2008; *Pancheva et al*., 2010]. *Pancheva and Mukhtarov* [2010] presented unambiguous evidence that the ionospheric DE3 variability is forced from below. Later, in *Mukhtarov and Pancheva* [2011], on the basis of global electron density data from COSMIC satellites, the authors found the main spatial structure and temporal variability of the electron density DE3 tide which have been supported by the whole atmosphere-ionosphere coupling GAIA model [*Pancheva et al*., 2012]. We pay special attention to the TEC DE3 nonmigrating diurnal component as it has the main contribution to the so-called wave number 4 (WN4) longitude structure observed in many ionospheric parameters particularly during low solar activity [*Immel et al*., 2006]. The other longitude wave-like structure, observed mainly in December solstice conditions, is the WN3 structure; the main contributor for it is the nonmigrating DE2 tide that forced the ionospheric DE2 variability [*Mukhtarov and Pancheva*, 2011]. Later, we will demonstrate the ability of this background model to reproduce the WN4 and WN3 ionospheric structures.

4. Model Results

[25] The basic aim of each global TEC model used for long-term prediction is to construct the global distribution of the TEC, i.e., to obtain global TEC maps, at given solar activity, DOY, and UT. The TEC maps are constructed by interpolation of the TEC values from the used grid with a 5° step in modip latitude and 15° in longitude. The interpolation between obtained from the model TEC values is done by using Inverse Distance to a Power Method. This gridding method is a weighted average interpolator that can be either an exact or a smoothing interpolator. The data points are weighted during interpolation such that the influence of one data point relative to another declines with distance from the grid node. Weighting is assigned to data points through the use of a weighting power that controls how the weighting factors drop off as distance from a grid node increases. The greater the weighting power the less effect points far from the grid node has during interpolation. For a smaller power, the weights are more evenly distributed among the neighboring data points [*Shepard*, 1968]. After completing the interpolation, the modip frame is converted to geographical one. The TEC values assigned to both poles are found by interpolation between the known from the model points which have the highest northern and southern latitudes. The model maps are arrayed in terms of the coordinate system of geographical latitude from −90° to 90° at each 5° and longitude from −180° to 180° at each 5°.

[26] First we will show how the background TEC model describes the WSA. The zone of anomalous diurnal variations in *foF2*, which is characterized by an excess of nighttime *foF2* values over daytime ones, occupies the longitudes of 0°–180°W and the latitudes of 40°–80°S as the effect is maximal (up to ~5 MHz for the critical frequency

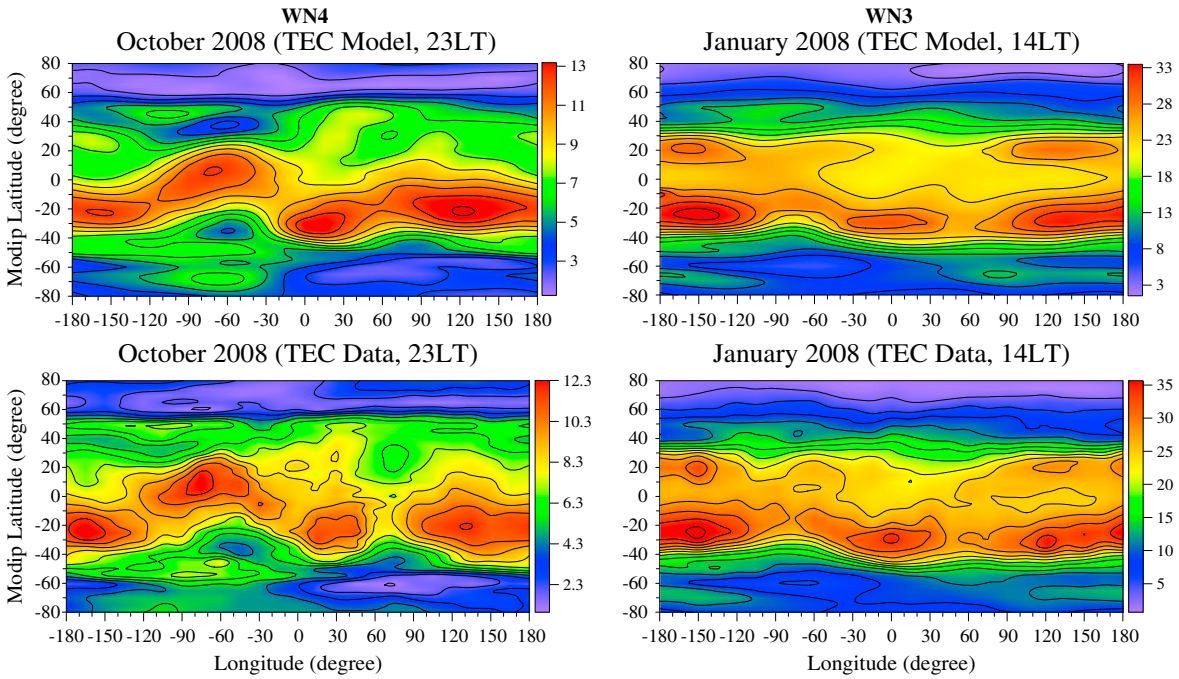

Figure 4. Comparison between the global TEC model maps in modip latitude (upper row of plots) and CODE TEC maps (bottom row of plots) which shows the ionospheric WN4 (left column of plots, at 23 UT for 15 October 2008) and WN3 (right column of plots, at 14 UT for 15 January 2008) structures.

of the *F* region, foF_2) at longitudes of 40°–105°W and latitudes of 60°–70°S [*Karpachev et al*., 2011]. Figure 3 presents the global map in geographical coordinate system calculated from the empirical background TEC model (upper plot) and compared with the CODE TEC map (bottom plot) at 08UT for 12 December 2012. The stripe TEC amplification in the Western Hemisphere at latitudes of ~50–80°S, i. e., the WSA, can be clearly distinguished at both model and CODE TEC maps; the maximal effect at both maps is near 70°S and longitudes of ~0–120°W. The presence of the WSA is a reason for appearing of an additional to the EIA TEC amplification around 30–40°S and at the most Western Hemisphere; this feature is also well reproduced by the model. The model TEC map describes well also the hemispheric asymmetry of the EIA revealing that the summer crest is stronger than the winter one.

[27] To demonstrate how the model reproduces some longitude wave-like structures, we re-arrayed the model and CODE TEC data sets in LT. It has been already mentioned that usually the ionospheric wave-like longitude structures are observed during low solar activity as the WN4 is seen in August–October, while the WN3 in December–January. Figure 4 shows the comparison between the global TEC model maps in modip latitude (upper row of plots) and CODE TEC maps (bottom row of plots) which represent the ionospheric WN4 (left column of plots) and WN3 (right column of plots) structures. The example for the WN4 structure is for October 2008 at 23LT, i.e., nighttime, and that is why there is no splitting of the irregularities at both sides of the equator. Four peaks around longitudes: −150°, −60°, 30°, and 120° can be clearly distinguished at both model and CODE TEC maps. There is not only qualitative but also quantitative similarity between the model and observations. The example for the WN3 structure is for January 2008 at 14LT, i.e., daytime, when the EIA is present. The splitting of the irregularities at both sides of the equator is seen at both model and CODE TEC maps. However, the WN3 structure is well developed and significantly stronger in SH. This hemispheric asymmetry is due to the asymmetry of the ionospheric DE2 variability, reported by *Mukhtarov and Pancheva* [2011], which is the main contributor of the WN3 structure. The three peaks particularly in the SH are located at longitudes of −150°, 0°, and 120°. They are not exactly equidistant most probably because the contribution of other nonmigrating tides, as DW4 and SE1, and SPW3 [*Pancheva and Mukhtarov*, 2012]. There are some signatures for the first and third peaks at NH evident at both model and CODE TEC maps.

[28] The ability of the background TEC model to reproduce the temporal-spatial feature of the input CODE TEC data will be displayed by a comparison between the model and CODE TEC maps for different solar activity, seasons and UT. While Figure 5a shows the global maps in geographical coordinate system calculated from the empirical background TEC model (left column of plots) which are compared with the CODE TEC maps (right column of plots) at 12UT for 15 January 2001 (upper row of plots) and 15 March 2001 (bottom row of plots) during high solar activity 2001, Figure 5b shows the same but during low solar activity 2008. The modip latitude is also marked at the plots by white line as the low-latitude plasma bulk follows the modip frame. At both solar cycle conditions, it is seen that the model maps reproduce very well the main features of the CODE TEC maps; some quantitative difference is evident only at winter model map where the EIA is slightly weaker than that at the CODE TEC map (Figure 5a, upper row of plots). The

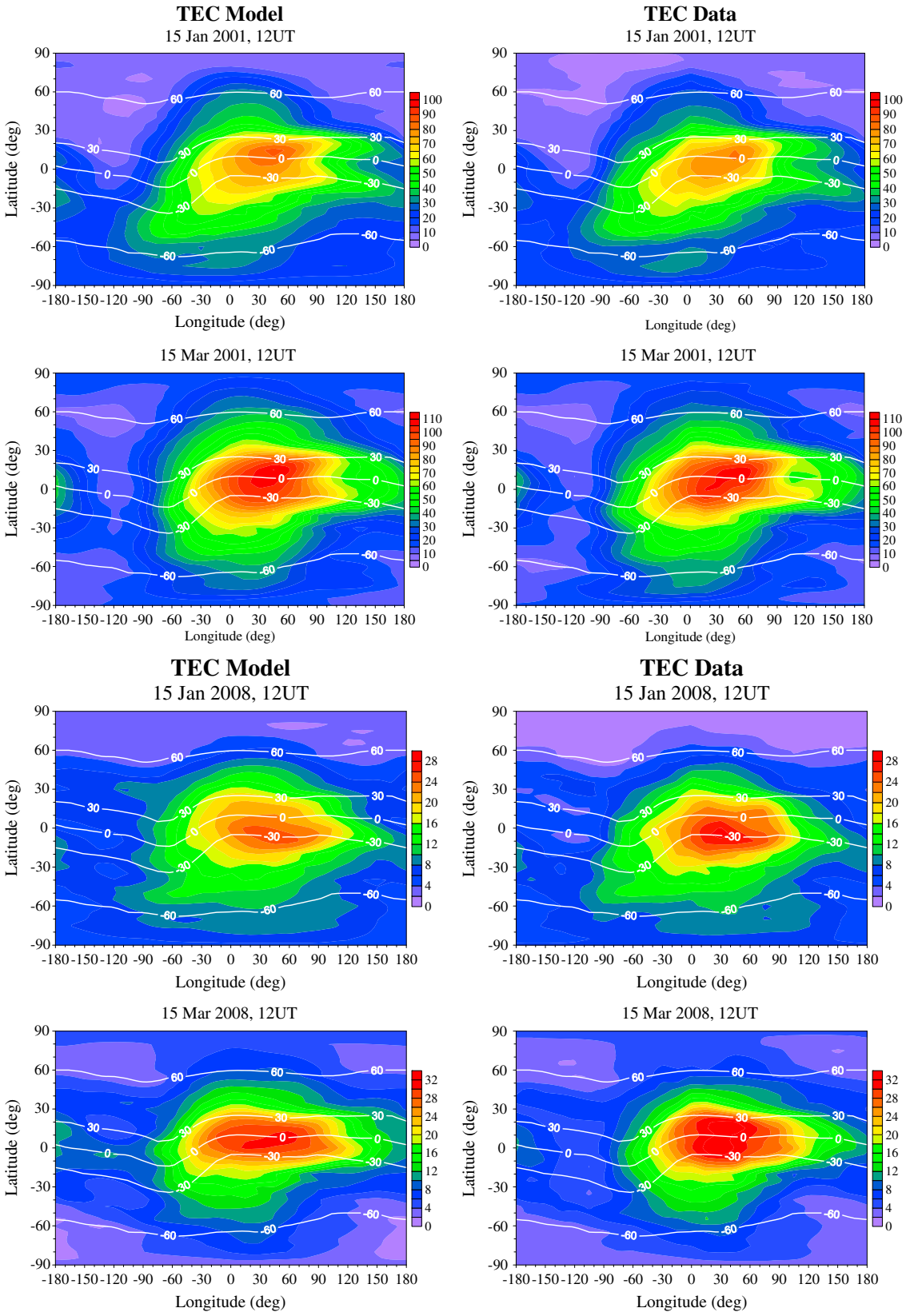

Figure 5. **(a)** Global maps in geographical coordinate system calculated from the empirical background TEC model (left column of plots) which are compared with the CODE TEC maps (right column of plots) at 12 UT for 15 January 2001 (upper row of plots) and 15 March 2001 (bottom row of plots) during high solar activity 2001. The modip latitude is also marked by white line. **(b)** The same as in Figure 5a, but during low solar activity 2008.

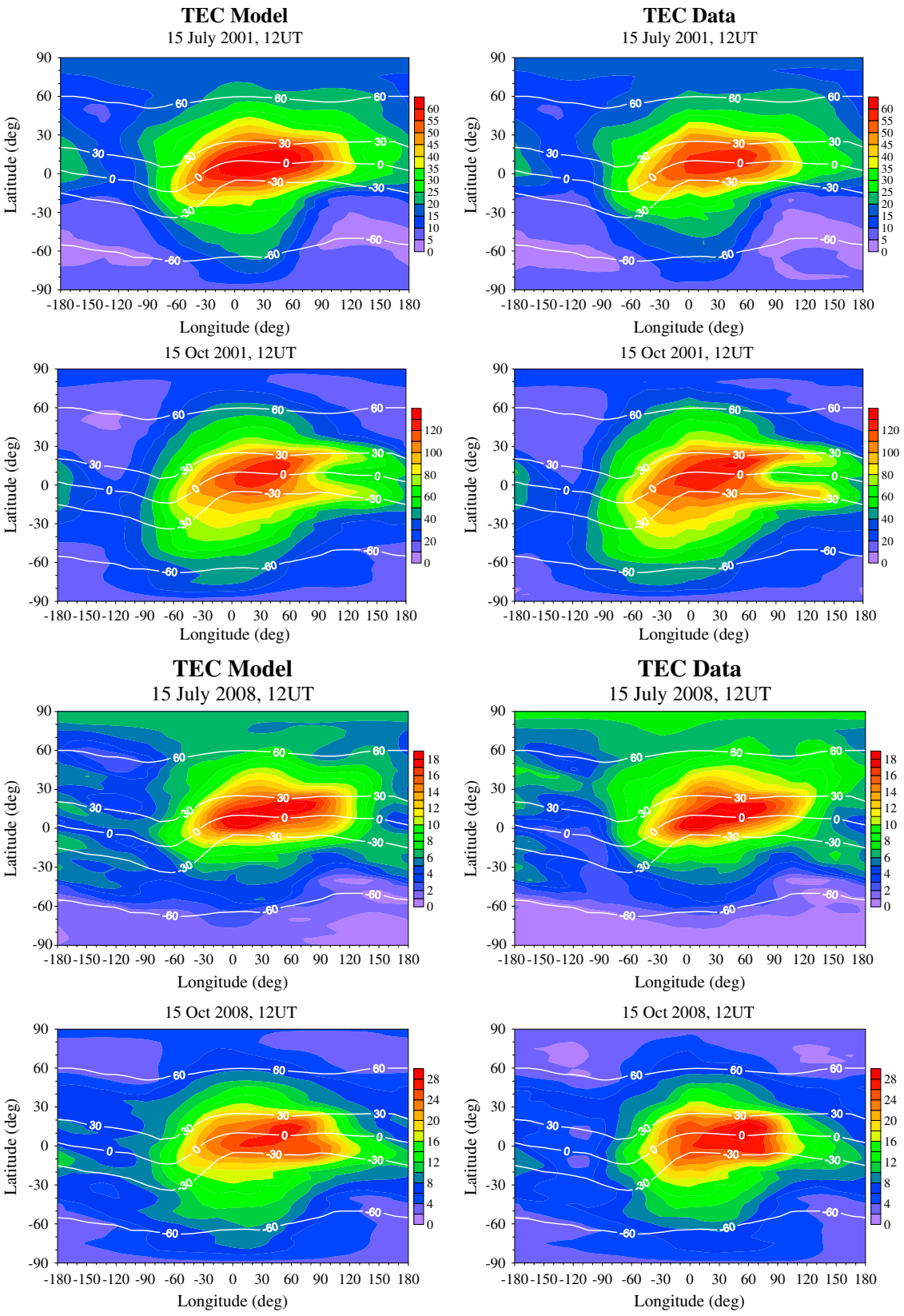

Figure 6. **(a)** Global maps in geographical coordinate system calculated from the empirical background TEC model (left column of plots) which are compared with the CODE TEC maps (right column of plots) at 12 UT for 15 July 2001 (upper row of plots) and 15 October 2001 (bottom row of plots) during high solar activity 2001. The modip latitude is also marked by white line. **(b)** The same as in Figure 6a, but during low solar activity 2008.

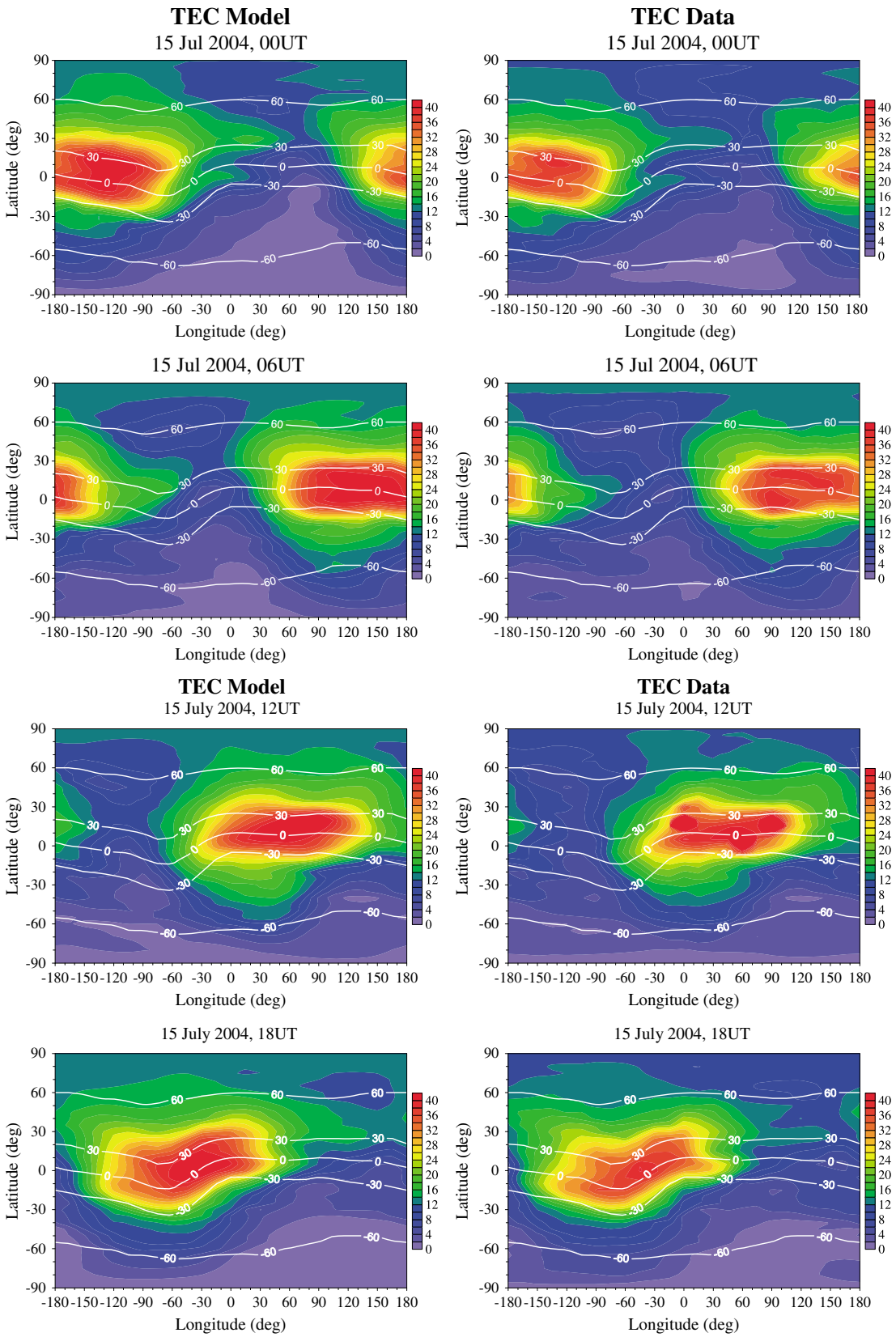

Figure 7. **(a)** Global maps in geographical coordinate system calculated from the empirical background TEC model (left column of plots) which are compared with the CODE TEC maps (right column of plots) at 00 UT (upper row of plots) and 06 UT (bottom row of plots) for 15 July 2004 during middle solar activity (2004). The modip latitude is also marked by white line. **(b)** The same as in Figure 7a, but at 12 UT (upper row of plots) and at 18 UT (bottom row of plots).

hemispheric asymmetry of the EIA, generated mainly by the thermospheric transequatorial neutral winds blowing from the summer to winter hemisphere, is evident well at both model and CODE maps but only at low solar activity (Figure 5b, upper row of plots). The hemispheric symmetry of the EIA during vernal equinox is also well evident at both model and CODE maps during high and low solar activity (Figures 5a and 5b, bottom rows of plots).

[29] Figure 6a presents the global maps from the background TEC model (left column of plots) compared with the CODE TEC maps (right column of plots) at 12UT for 15 July 2001 (upper row of plots) and 15 October 2001 (bottom row of plots) during high solar activity 2001, while Figure 6b shows the same but for low solar activity 2008. Again, the degree of similarity between model and CODE TEC maps is very high. Some underestimation of the model TEC is seen in July at most northern latitudes at both high and low solar activity (Figures 6a and 6b, upper row of plots). The model, however, reproduces very well the four TEC amplifications seen between ~50°N and ~40°S at the most western longitudes and two TEC amplifications at most eastern longitudes in July 2008 (Figure 6b, upper row of plots). It is worth noting that both model and CODE maps show the following features: (i) do not display hemispheric asymmetry of the EIA during July at both solar activity conditions, (ii) the January TEC is larger than that in July at high and low solar activity (so-called winter anomaly), and (iii) while the March TEC is higher than the October one during low solar activity, the opposite feature is evident during high solar activity. The last result does not support that of *Natali and Meza* [2011] which however is found for 2000 (not 2001 as here). We remind also that all the above mentioned features are seen at 12UT.

[30] The comparisons for the middle solar activity 2004 are presented in Figures 7a and 7b; in this case, only maps for July at different UT are shown in order to trace out better the diurnal variability of the low latitude plasma bulk. Figure 7a shows global maps from the background TEC model (left column of plots) which are compared with the CODE TEC maps (right column of plots) at 00UT (upper row of plots) and 06UT (bottom row of plots) for 15 July 2004 while Figure 7b presents the same but at 12UT (upper row of plots) and at 18UT (bottom row of plots). Again the comparison shows high degree of similarity; even some details in the spatial TEC distribution are well reproduced (see, for example, Figure 7a). Some hemispheric asymmetry of the whole low-latitude plasma bulk can be distinguished only at 00UT and 18UT; the TEC values at positive modip latitudes are larger than those at the respective negative ones.

[31] The above shown comparisons indicate that the empirical background TEC model can reproduce very well the main spatial-temporal variability of the CODE TEC maps. Each empirical model needs to assess the quality of the adjustment procedure by model residuals, i.e., by calculating the differences between input data and model values [*Jakowski et al*., 2011]. A detailed description of the model residuals will be done in the companion paper. Here however only the main statistics based on the entire data set will be presented. It is worth noting that actually the residuals reveal the nature of the modelling error. Due to this, it has been accepted that the mean (systematic) error (*ME*), root mean squares error (*RMSE*), and the standard deviation error (*STDE*) are the main characteristics of each model. They are defined as:

$$ME = \frac{1}{N}\sum_{i=1}^{N}(TEC_{\mathrm{mod}} - TEC_{obs})$$

$$RMSE = \sqrt{\frac{1}{N}\sum_{i=1}^{N}(TEC_{\mathrm{mod}} - TEC_{obs})^2}$$

$$STDE = \sqrt{RMSE^2 - ME^2} \qquad (4)$$

[32] The application of (4) to all data for the considered period of time (1 January 1999–31 December 2011) gives the following errors: $ME = 0.003$ TECU, i.e., the model has practically zero systematic error. In this case, $RMSE = STDE = 3.387$ TECU. In order to have an idea if such errors are high or low, we compare this model with the similar to some extend new global TEC model built recently by *Jakowski et al*. [2011] and called NTCM-GL model. The statistical assessments of the NTCM-GL model are: $ME = -0.3$ TECU and $RMSE = 7.5$ TECU. Hence, the errors of the present background TEC model are significantly smaller than those of the NTCM-GL model. We have to note nevertheless that both models are climatological, i.e., they describe the average behavior under quiet geomagnetic conditions, the TEC model constructed by *Jakowski et al*. [2011] needs only 12 coefficients and a few empirically fixed parameters for describing a broad spectrum of TEC variation at all levels of solar activity. We, however, do not consider the large number of coefficients in the present background TEC model, 4374, as its weak point. They are calculated only once and are fixed later at the model applications.

5. Summary

[33] In this study, we present a global background TEC model built on the basis of full 13 years (1999–2011) of CODE TEC data. The model describes the climatological, i.e., under quiet geomagnetic conditions, behavior of the ionosphere, and can be used for long-term prediction. For this purpose, at given DOY, geographic location, and UT, the model needs as input parameters only the predicted level of solar activity (F10.7 is used here as a proxy for solar activity). The model maps are arrayed in terms of the coordinate system of geographical latitude from −90° to 90° at each 5° and longitude from −180° to 180° at each 5°.

[34] The approach for building this model is based on the very different time scales of the solar cycle, seasonal, and diurnal TEC variabilities (they differ at least an order of magnitude). This leads to modulations of shorter-period variabilities with periods of the longer ones. Then the TEC spatial-temporal variability has been presented as a multiplication of three separable functions (as it is shown in (2)). In constructing the present background model, besides the seasonal course that is described in a standard way, i.e., by the subharmonics of the year, the two new ideas are used in empirical modeling of the TEC solar cycle and diurnal variabilities:

[35] 1. solar cycle variability is presented not only by F10.7 but also by its linear rate of change, K_F, i.e., its tendency; in this way, the model describes better the different ionospheric behavior at rising and declining parts of the solar cycle when F10.7 has the same values;

[36] 2. diurnal TEC variability is described not only by migrating tidal components, as it has been done so far, but nonmigrating tides and SPW structures are also included; in this way, the contribution of both tidal forcing from below and the effects arising from the offset between geographic and modip latitudes are included in the model.

[37] It was shown that the model describes very well such structures as the WSA (Figure 3) and the well-known WN4 and WN3 longitude structures (Figure 4). This was possible mainly because of the nonmigrating tides and SPW inclusion in describing the diurnal variability of the TEC. The presented comparison between the model and CODE TEC maps at different solar activities and seasons (Figures 5, 6, and 7) also demonstrated high degree of similarity. The zero systematic error and its low *RMSE* (3.387 TECU) provides the model significant advantage over the other similar models. The detailed statistical evaluation of the present model will be done in the companion paper. There, an error model will be presented as well.

[38] The present background model can be used for both science and applications. In science, the model can be utilized as a background condition on the basis of which the perturbations can be estimated. It is particularly useful for investigating the geomagnetic perturbations, or ionospheric disturbances related to the sudden stratospheric warmings, by incoherent scatter radars where the measurements are available only for several days; in this case, the background condition described by the monthly median TEC values cannot be determined. This model can be useful for numerous single-frequency GPS applications which need additional information for mitigating the ionospheric propagation error. Such GNSS users can be provided by adequate ionospheric corrections obtained by this autonomous ionospheric TEC model.

[39] **Acknowledgments.** We are grateful to the CODE TEC team for the access to the TEC data provided from the CODE FTP directory: ftp://ftp.unibe.ch/aiub/CODE/. This work was supported by the European Office of Aerospace Research and Development (EOARD), Air Force Office of Scientific Research, Air Force Material Command, USAF, under grant FA8655-12-1-2057 to D. Pancheva. We thank the anonymous reviewers for their insightful comments on the original manuscript.

[40] Robert Lysak thanks the reviewers for their assistance in evaluating this paper.

References

Anderson, D. N., J. M. Forbes, and M. Codrescu (1989), A fully analytical, low- and middle-latitude ionospheric model, *J. Geophys. Res.*, *94*(A2), 1520–1524, doi:10.1029/JA094iA02p01520.

Apostolov, E., L. Alberca, and D. Pancheva (1994), Long-term prediction of the foF2 on the rising and falling parts of the solar cycle, *Adv. Space Res.*, *14*(12), 47–50.

Azpilicueta, F., C. Brunini, and S. M. Radicella (2006), Global ionospheric maps from GPS observations using modip latitude, *Adv. Space Res.*, *38*, 2324–2331.

Bilitza, D. (2001), International Reference Ionosphere 2000, *Radio Sci.*, *36*, 261–275, doi:10.1029/2000RS002432.

Bilitza, D., and B. W. Reinisch (2008), International Reference Ionosphere 2007: Improvements and new parameters, *Adv. Space Res.*, *42*, 599–609, doi:10.1016/j.asr.2007.07.048.

Bouya, Z., M. Terkildsen, and D. Neudegg (2010), Regional GPS-based ionospheric TEC model over Australia using Spherical Cap Harmonic Analysis, paper presented at 38th COSPAR Scientific Assembly, Comm. on Space Res., Bremen, Germany.

Brunner, F. K., and M. Gu (1991), An improved model for the dual frequency ionospheric correction of GPS observations, *Manuscr. Geodaet.*, *16*, 205–214.

Chen, C. H., J. D. Huba, A. Saito, C. H. Lin, and J. Y. Liu (2011), Theoretical study of the ionospheric Weddell Sea Anomaly using SAMI2, *J. Geophys. Res.*, *116*, A04305, doi:10.1029/2010JA015573.

Daniell, R. E., W. G. Whartenby, and L. D. Brown (1993a), Parameterized Real-time Ionospheric Specification Model, PRISM version 1.2, Algorithm description, Comput. Phys., Inc., Newton, Mass.

Daniell, R. E., W. G. Whartenby, and L. D. Brown (1993b), Parameterized Real-time Ionospheric Specification Model, PRISM version 1.2, Validation report, Comput. Phys., Inc., Newton, Mass.

Dow, J. M., R. E. Neilan, and C. Rizos (2009), The International GNSS Service in a changing landscape of Global Navigation Satellite Systems, *J. Geod.*, *83*, 191–198, doi:10.1007/s00190-008-0300-3.

Drob, D. P., et al. (2008), An empirical model of the Earth's horizontal wind fields: HWM07, *J. Geophys. Res.*, *113*, A12304, doi:10.1029/2008JA013668.

Elmas, Z. G., M. Aquino, H. A. Marques, and J. F. G. Monico (2011), Higher order ionospheric effects in GNSS positioning in the European region, *Ann. Geophys.*, *29*, 1383–1399, doi:10.5194/angeo-29-1383-2011.

Ercha, A., D. Zhang, A. J. Ridley, Z. Xiao, and Y. Hao (2012), A global model: Empirical orthogonal function analysis of total electron content 1999–2009 data, *J. Geophys. Res.*, *117*, A03328, doi:10.1029/2011JA017238.

Feltens, J. (2007), Development of a new three-dimensional mathematical ionosphere model at European Space Agency/European Space Operations Centre, *Space Weather*, *5*, S12002, doi:10.1029/2006SW000294.

Feltens, J., and S. Schaer (1998), IGS products for the ionosphere, *IGS Position Paper*, in *IGS 1998 Analysis Center Workshop: Proceedings*, edited by J. M. Dow, J. Kouba, and T. Springer, pp. 225–232, Eur. Space Oper. Cent., Darmstadt, Germany.

Feltens, J., M. Angling, N. Jackson-Booth, N. Jakowski, M. Hoque, M. Hernández-Pajares, A. Aragón-Àngel, R. Orús, and R. Zandbergen (2011), Comparative testing of four ionospheric models driven with GPS measurements, *Radio Sci.*, *46*, RS0D12, doi:10.1029/2010RS004584.

Fuller-Rowell, T. J., D. Rees, S. Quegan, R. J. Moffett, and G. J. Bailey (1987), Interaction between neutral thermosphere composition and the polar ionosphere using a coupled ionosphere-thermosphere model, *J. Geophys. Res.*, *92*(A7), 7744–7748, doi:10.1029/JA092iA07p07744.

Fuller-Rowell, T., E. Araujo-Pradere, C. Minter, M. Codrescu, P. Spencer, D. Robertson, and A. R. Jacobson (2006), US-TEC: A new data assimilation product from the Space Environment Center characterizing the ionospheric total electron content using real-time GPS data, *Radio Sci.*, *41*, RS6003, doi:10.1029/2005RS003393.

Gao, Y., and Z. Z. Liu (2002), Precise ionosphere modeling using regional GPS network data, *J. Global Pos. Systems*, *1*, 18–24.

Gao, Y., P. Heroux, and J. Kouba (1994), Estimation of GPS receiver and satellite L1/L2 signal delay biases using data from CACS, paper presented at the International Symposium on Kinematic Systems in Geodesy, Geomatics, and Navigation, Univ. of Calgary, Banff, Alberta, Canada.

Ge, S., et al. (2004), Comparison of TEC measurements from dual frequency space geodetic techniques, *Eos. Trans. AGU*, *85*(47), Fall Meet. Suppl., Abstract G53A-0118.

Gopal Rao, M. S. V., and R. Sambasiva Rao (1969), The hysteresis variation in the F2-layer parameters, *J. Atmos. Terr. Phys.*, *31*, 1119–1125.

Habarulema, J. B., L.-A. McKinnell, and B. D. L. Opperman (2010), TEC measurements and modelling over Southern Africa during magnetic storms; a comparative analysis, *J. Atmos. Sol. Terr. Phys.*, *72*, 509–520, doi:10.1016/j.jastp.2010.01.012.

Habarulema, J. B., L.-A. McKinnell, and B. D. L. Opperman (2011), Regional GPS TEC modeling; Attempted spatial and temporal extrapolation of TEC using neural networks, *J. Geophys. Res.*, *116*, A04314, doi:10.1029/2010JA016269.

Hartman, W. A., and R. A. Heelis (2007), Longitudinal variations in the equatorial vertical drift in the topside ionosphere, *J. Geophys. Res.*, *112*, A03305, doi:10.1029/2006JA011773.

He, M., L. Liu, W. Wan, B. Ning, B. Zhao, J. Wen, X. Yue, and H. Le (2009), A study of the Weddell Sea Anomaly observed by FORMOSAT-3/COSMIC, *J. Geophys. Res.*, *114*, A12309, doi:10.1029/2009JA014175.

Hedin, A. E., et al. (1996), Empirical wind model for the upper, middle and lower atmosphere, *J. Atmos. Terr. Phys.*, *58*, 1421–1447.

Hernández-Pajares, M., J. M. Juan, and J. Sanz (1997), High-resolution TEC monitoring method using permanent ground GPS receivers, *Geophys. Res. Lett.*, *24*, 1643–1646, doi:10.1029/97GL01591.

Hernández-Pajares, M., J. M. Juan, and J. Sanz (1999), New approaches in global ionospheric determination using ground GPS data, *J. Atmos. Sol. Terr. Phys.*, *61*, 1237–1247, doi:10.1016/S1364-6826(99)00054-1.

Hernández-Pajares, M., J. M. Juan, J. Sanz, R. Orus, A. Garcia-Rigo, J. Feltens, A. Komjathy, S. C. Schaer, and A. Krankowski (2009), The IGS VTEC maps: A reliable source of ionospheric information since 1998, *J. Geod.*, *83*, 263–275, doi:10.1007/s00190-008-0266-1.

Ho, C. M., A. J. Mannucci, U. J. Lindqwister, X. Pi, and B. T. Tsurutani (1996), Global ionosphere perturbations monitored by the worldwide GPS network, *Geophys. Res. Lett.*, *23*, 3219–3222, doi:10.1029/1996GL02763.

Hochegger, G., B. Nava, S. M. Radicella, and R. Leitinger (2000), A family of ionospheric models for different uses, *Phys. Chem. Earth C Sol. Terr. Planet. Sci.*, *25*(4), 307–310.

Hoque, M. M., and N. Jakowski (2007), Higher order ionospheric effects in precise GNSS positioning, *J. Geod.*, *81*(4), 259–268, doi:10.1007/s00190-006-0106-0.

Huang, J.-N. (1963), The hysteresis variation of the semi-thickness of the F2-layer and its relevant phenomena at Kokubunji, Japan, *J. Atmos. Terr. Phys.*, *25*, 647–658.

Huba, J. D., G. Joyce, S. Sazykin, R. Wolf, and R. Spiro (2005), Simulation study of penetration electric field effects on the low- to mid-latitude ionosphere, *Geophys. Res. Lett.*, *32*, L23101, doi:10.1029/2005GL024162.

Iijima, B. A., I. L. Harris, C. M. Ho, U. J. Lindqwister, A. J. Mannucci, X. Pi, M. J. Reyes, L. C. Sparks, and B. D. Wilson (1999), Automated daily process for global ionospheric total electron content maps and satellite ocean altimeter ionospheric calibration based on Global Positioning System data, *J. Atmos. Sol. Terr. Phys.*, *61*, 1205–1218, doi:10.1016/S1364-6826(99)00067-X.

Immel, T. J., E. Sagawa, S. L. England, S. B. Henderson, M. E. Hagan, S. B. Mende, H. U. Frey, C. M. Swenson, and L. J. Paxton (2006), Control of equatorial ionospheric morphology by atmospheric tides, *Geophys. Res. Lett.*, *33*, L15108, doi:10.1029/2006GL026161.

Jakowski, N., M. M. Hoque, and C. Mayer (2011), A new global TEC model estimating trans-ionospheric radio wave propagation errors, *J. Geod.*, *85*, 965–974, doi:10.1007/s00190-011-0455-1.

Karpachev, A. T., N. A. Gasilov, and O. A. Karpachev (2011), Morphology and causes of the Weddel Sea Anomaly, *Geomag. Aeron.*, *51*(6), 812–824, doi:10.1134/S0016793211050070.

Kashcheyev, A., B. Nava, and S. M. Radicella (2012), Estimation of higher-order ionospheric errors in GNSS positioning using a realistic 3-D electron density model, *Radio Sci.*, *47*, RS4008, doi:10.1029/2011RS004976.

Kil, H., E. R. Talaat, S.-J. Oh, L. J. Paxton, S. L. England, and S.-Y. Su (2008), The wave structures of the plasma density and vertical E × B drift in low-latitude F region, *J. Geophys. Res.*, *113*, A09312, doi:10.1029/2008JA013106.

Komjathy, A. (1997), Global ionospheric total electron content mapping using the Global Positioning System, Ph.D. thesis, Univ. of New Brunswick, Frederiction, New Brunswick, Canada.

Lean, J. L., R. R. Meier, J. M. Picone, and J. T. Emmert (2011a), Ionospheric total electron content: Global and hemispheric climatology, *J. Geophys. Res.*, *116*, A10318, doi:10.1029/2011JA016567.

Lean, J. L., J. T. Emmert, J. M. Picone, and R. R. Meier (2011b), Global and regional trends in ionospheric total electron content, *J. Geophys. Res.*, *116*, A00H04, doi:10.1029/2010JA016378.

Lean, J. L., T. N. Woods, F. G. Eparvier, R. R. Meier, D. J. Strickland, J. T. Correira, and J. S. Evans (2011c), Solar extreme ultraviolet irradiance: Present, past, and future, *J. Geophys. Res.*, *116*, A01102, doi:10.1029/2010JA015901.

Mannucci, A. J., B. D. Wilson, D. N. Yuan, C. H. Ho, U. J. Lindqwister, and T. F. Runge (1998), A global mapping technique for GPS-derived ionospheric total electron content measurements, *Radio Sci.*, *33*, 565–582, doi:10.1029/97RS02707.

Mao, T., W. Wan, X. Yue, L. Sun, B. Zhao, and J. Guo (2008), An empirical orthogonal function model of total electron content over China, *Radio Sci.*, *43*, RS2009, doi:10.1029/2007RS003629.

Meggs, R. W., C. N. Mitchell, and P. S. J. Spencer (2004), A comparison of techniques for mapping total electron content over Europe using GPS signals, *Radio Sci.*, *39*, RS1S10, doi:10.1029/2002RS002846.

Mendillo, M., H. Rishbeth, R. G. Roble, and J. Wroten (2002), Modelling F2-layer seasonal trends and day-to-day variability driven by coupling with the lower atmosphere, *J. Atmos. Sol. Terr. Phys.*, *64*, 1911–1931, doi:10.1016/S1364-6826(02)00193-1.

Mukhtarov, P. and D. Pancheva (2011), Global ionospheric response to nonmigrating DE3 and DE2 tides forced from below, *J. Geophys. Res.*, *116*, A05323, doi:10.1029/2010JA016099.

Mukhtarov, P., D. Pancheva, and B. Andonov (2010), Climatology of the stationary planetary waves seen in the SABER/TIMED temperatures (2002–2007), *J. Geophys. Res.*, *115*, A06315, doi:10.1029/2009JA015156.

Natali, M. P., and A. Meza (2011), Annual and semiannual variations of vertical total electron content during high solar activity based on GPS observations, *Ann. Geophys.*, *29*, 865–873.

Nava, B., P. Coisson, and S. M. Radicella (2008), A new version of the NeQuick ionosphere electron density model, *J. Atmos. Sol. Terr. Phys.*, *70*, 1856–1862.

Oberheide, J., and J. M. Forbes (2008), Tidal propagation of deep tropical cloud signatures into the thermosphere from TIMED observations. *Geophys. Res. Lett. 35*, L04816, doi:10.1029/ 2007GL032397.

Oberheide, J., J. M. Forbes, X. Zhang, and S. L. Bruinsma (2011), Wave-driven variability in the ionosphere-thermosphere-mesosphere system from TIMED observations: What contributes to the "wave4"?, *J. Geophys. Res.*, *116*, A01306, doi:10.1029/2009JA015911.

Orús, R., M. Hernández-Pajares, J. M. Juan, and J. Sanz (2005), Improvement of global ionospheric VTEC maps by using Kriging interpolation technique, *J. Atmos. Sol. Terr. Phys.*, *67*, 1598–1609, doi:10.1016/j.jastp.2005.07.017.

Otsuka, Y., et al. (2002), A new technique for mapping of total electron content using GPS network in Japan, *Earth Planet Space*, *54*, 63–70.

Pancheva, D., and P. Mukhtarov (1996), A single-station spectral model of the monthly median F-region critical frequency, *Ann. Geofisc.*, *39*(4), 807–818.

Pancheva, D., and P. Mukhtarov (1998), A single station spectral model of the monthly median foF2 and M(3000)F2, *Studia geophys. et geod.*, *42*(2), 183–196, doi:10.1023/A:1023361105552.

Pancheva D., and P. Mukhtarov (2010), Strong evidence for the tidal control on the longitudinal structure of the ionospheric F-region, *Geophys. Res. Lett.*, *37*, L14105, doi:10.1029/ 2010GL044039.

Pancheva, D., and P. Mukhtarov (2012), Global response of the ionosphere to atmospheric tides forced from below: Recent progress based on satellite measurements, *Space Sci. Rev.*, *168*(1–4), 175–209, doi:10.1007/s11214-011-9837-1.

Pancheva, D., P. Mukhtarov, N. J. Mitchell, and H. G. Muller (2005), Empirical Model of the Dynamics in the Mesosphere and Lower Thermosphere Region over the UK, Including Solar and Geomagnetic Activity, *J. Atmos. Sol. Terr. Phys.*, *67*, 197–209.

Pancheva, D., P. Mukhtarov, and B. Andonov (2010), Climatology of the eastward propagating tides seen in the SABER/TIMED temperatures (2002–2007), *Adv. Space Res.*, *46*, 257–274, doi:10.1016/j.asr.2010.03.026.

Pancheva, D., Y. Miyoshi, P. Mukhtarov, H. Jin, H. Shinagava, and H. Fujiwara (2012), Global response of the ionosphere to atmospheric tides forced from below: Comparison between COSMIC measurements and simulations by Atmosphere–ionosphere Coupled Model GAIA, *J. Geophys. Res.*, *117*, A07319, doi:10.1029/2011JA017452.

Ping, J., Y. Kono, K. Matsumoto, Y. Otsuka, A. Saito, C. Shum, K. Heki, and N. Kawano (2002), Regional ionosphere map over Japanese Islands, *Earth Planet. Space*, *54*, e13–e16.

Radicella, S. M., and R. Leitinger (2001), The evolution of the DGR approach to model electron density profiles, *Adv. Space Res.*, *27*, 35–40.

Rawer, K. (1963), in *Meteorological and Astronomical Influences on Radio Wave Propagation*, edited by B. Landmark, pp. 221–250, Pergamon Press, Oxford.

Rawer, K. (1984), (Ed.), *Encyclopedia of Physics, Geophysics III, Part VII*, pp. 389–391, Springer-Verlag, Berlin.

Ren, Z., W. Wan, L. Liu, B. Zhao, Y. Wei, X. Yue, and R. A. Heelis (2008), Longitudinal variations of electron temperature and total ion density in the sunset equatorial topside ionosphere, *Geophys. Res. Lett.*, *35*, L05108, doi:10.1029/2007GL032998.

Rishbeth, H. (2006), F region links with the lower atmosphere?, *J. Atmos. Sol. Terr. Phys.*, *68*, 469–478, doi:10.1016/j.jastp.2005.03.017.

Roble, R. (1995), Energetics of the mesosphere and thermosphere, in *The Upper Mesosphere and Lower Thermosphere: A Review of Experiment and Theory*, Geophys. Monogr. Ser., vol. 87, edited by R. M. Johnson and T. L. Killeen, pp. 1–22, AGU, Washington, D. C., doi:10.1029/GM087.

Sayin, I., F. Arikan, and O. Arikan (2008), Regional TEC mapping with Random Field Priors and Kriging, *Radio Sci.*, *43*, RS5012, doi:10.1029/2007RS003786.

Schaer, S. (1999), *Mapping and Predicting the Earth's Ionosphere Using the Global Positioning System*, vol. 59, Geod. Geophys. Arb. Schweiz.Inst. für Geod. und Photogramm, Zurich, Switzerland.

Schunk, R. W., and A. F. Nagy (2009), *Ionospheres—Physics, Plasma Physics, and Chemistry*, 628 pp., Cambridge Univ. Press, New York, doi:10.1017/CBO9780511635342.

Schunk, R. W., J. J. Sojka, and M. D. Bowline (1986), Theoretical study of the electron temperature in the high latitude ionosphere for solar maximum and winter conditions, *J. Geophys. Res.*, *91*(A11), 12,041–12,054, doi:10.1029/JA091iA11p12041.

Shepard, D. (1968), A two-dimensional interpolation function for irregularly-spaced data, *ACM '68 Proc.*, pp. 517–524, ACM New York, New York, doi:10.1145/800186.810616.

Stolle, C., S. Schlüter, S. Heise, C. Jacobi, N. Jakowski, S. Friedel, D. Kürschner, and H. Lühr (2005), GPS ionospheric imaging of the north polar ionosphere on 30 October 2003, *Adv. Space Res.*, *36*, 2201–2206, doi:10.1016/j.asr.2005.08.047.

Wan, W., L. Liu, X. Pi, M.-L. Zhang, B. Ning, J. Xiong, and F. Ding (2008), Wavenumber-4 patterns of the total electron content over the low latitude ionosphere, *Geophys. Res. Lett.*, *35*, L12104, doi:10.1029/2008GL033755.

Wan, W., F. Ding, M. Zhang, L. Liu, and B. Ning (2012), Modeling the global ionospheric total electron content with empirical orthogonal function analysis, *Sci. China, Ser. E*, *55*, 1161–1168, doi:10.1007/s11431-012-4823-8.

Wilson, B. D., A. J. Mannucci, and C. D. Edwards (1995), Subdaily northern hemisphere maps using an extensive network of GPS receivers, *Radio Sci.*, *30*, 639.

Wu, Q., D. A. Ortland, S. C. Solomon, W. R. Skinner, and R. J. Niciejewski (2011), Global distribution, seasonal, and inter-annual variations of mesospheric semidiurnal tide observed by TIMED TIDI, *J. Atmos. Sol. Terr. Phys.*, *73*(17–18), 2482–2502, doi:10.1016/ j.jastp.2011.08.007.

Zapfe, B. D., M. Materassi, C. N. Mitchell, and P. Spalla (2006), Imaging of the equatorial ionospheric anomaly over South America—A simulation study of total electron content, *J. Atmos. Sol. Terr. Phys.*, *68*, 1819–1833.